



UNIVERSITÀ  
DEGLI STUDI  
FIRENZE

FLORE

## Repository istituzionale dell'Università degli Studi di Firenze

### **Biochemical and Electrophysiological Modification of Amyloid Transthyretin on Cardiomyocytes**

Questa è la Versione finale referata (Post print/Accepted manuscript) della seguente pubblicazione:

*Original Citation:*

Biochemical and Electrophysiological Modification of Amyloid Transthyretin on Cardiomyocytes / Sartiani, Laura; Bucciantini, Monica; Spinelli, Valentina; Leri, Manuela; Natalello, Antonino; Nosi, Daniele; Maria Doglia, Silvia; Relini, Annalisa; Penco, Amanda; Giorgetti, Sofia; Gerace, Elisabetta; Mannaioni, Guido; Bellotti, Vittorio; Rigacci, Stefania; Cerbai, Elisabetta; Stefani, Massimo. - In: BIOPHYSICAL JOURNAL. - ISSN

*Availability:*

The webpage <https://hdl.handle.net/2158/1059024> of the repository was last updated on 2017-03-28T15:03:28Z

*Published version:*

DOI: 10.1016/j.bpj.2016.09.010

*Terms of use:*

Open Access

La pubblicazione è resa disponibile sotto le norme e i termini della licenza di deposito, secondo quanto stabilito dalla Policy per l'accesso aperto dell'Università degli Studi di Firenze (<https://www.sba.unifi.it/upload/policy-oa-2016-1.pdf>)

*Publisher copyright claim:*

La data sopra indicata si riferisce all'ultimo aggiornamento della scheda del Repository FloRe - The above-mentioned date refers to the last update of the record in the Institutional Repository FloRe

(Article begins on next page)

# Biochemical and Electrophysiological Modification of Amyloid Transthyretin on Cardiomyocytes

Laura Sartiani,<sup>1,2</sup> Monica Bucciantini,<sup>3,4,\*</sup> Valentina Spinelli,<sup>1,2</sup> Manuela Leri,<sup>3</sup> Antonino Natalello,<sup>5</sup> Daniele Nosi,<sup>6</sup> Silvia Maria Doglia,<sup>5</sup> Annalisa Relini,<sup>7</sup> Amanda Penco,<sup>7</sup> Sofia Giorgetti,<sup>8</sup> Elisabetta Gerace,<sup>9</sup> Guido Mannaioni,<sup>1</sup> Vittorio Bellotti,<sup>8,10</sup> Stefania Rigacci,<sup>3</sup> Elisabetta Cerbai,<sup>1,2,4</sup> and Massimo Stefani<sup>3,4</sup>

<sup>1</sup>Department of Neuroscience, Psychology, Drug Research and Child Health, <sup>2</sup>Center of Molecular Medicine, <sup>3</sup>Department of Biomedical, Experimental and Clinical Sciences "Mario Serio," and <sup>4</sup>Research Centre on the Molecular Basis of Neurodegeneration, University of Florence, Florence, Italy; <sup>5</sup>Department of Biotechnology and Biosciences, University of Milano-Bicocca, Milan, Italy; <sup>6</sup>Department of Experimental and Clinical Medicine, University of Florence, Florence, Italy; <sup>7</sup>Department of Physics, University of Genoa, Genoa, Italy; <sup>8</sup>Department of Molecular Medicine, Institute of Biochemistry, University of Pavia, Pavia, Italy; <sup>9</sup>Department of Health Science, University of Florence, Florence, Italy; and <sup>10</sup>Wolfson Drug Discovery Unit, Centre for Amyloidosis and Acute Phase Proteins, Division of Medicine, University College London, London, United Kingdom

**ABSTRACT** Transthyretin (TTR) amyloidoses are familial or sporadic degenerative conditions that often feature heavy cardiac involvement. Presently, no effective pharmacological therapy for TTR amyloidoses is available, mostly due to a substantial lack of knowledge about both the molecular mechanisms of TTR aggregation in tissue and the ensuing functional and viability modifications that occur in aggregate-exposed cells. TTR amyloidoses are of particular interest regarding the relation between functional and viability impairment in aggregate-exposed excitable cells such as peripheral neurons and cardiomyocytes. In particular, the latter cells provide an opportunity to investigate in parallel the electrophysiological and biochemical modifications that take place when the cells are exposed for various lengths of time to variously aggregated wild-type TTR, a condition that characterizes senile systemic amyloidosis. In this study, we investigated biochemical and electrophysiological modifications in cardiomyocytes exposed to amyloid oligomers or fibrils of wild-type TTR or to its T4-stabilized form, which resists tetramer disassembly, misfolding, and aggregation. Amyloid TTR cytotoxicity results in mitochondrial potential modification, oxidative stress, deregulation of cytoplasmic  $Ca^{2+}$  levels, and  $Ca^{2+}$  cycling. The altered intracellular  $Ca^{2+}$  cycling causes a prolongation of the action potential, as determined by whole-cell recordings of action potentials on isolated mouse ventricular myocytes, which may contribute to the development of cellular arrhythmias and conduction alterations often seen in patients with TTR amyloidosis. Our data add information about the biochemical, functional, and viability alterations that occur in cardiomyocytes exposed to aggregated TTR, and provide clues as to the molecular and physiological basis of heart dysfunction in sporadic senile systemic amyloidosis and familial amyloid cardiomyopathy forms of TTR amyloidoses.

## INTRODUCTION

In the past few years, misfolded proteins have been proposed to play a key role in the pathophysiology of several cardiac diseases in humans, including pathologic cardiac hypertrophy and dilated and ischemic cardiomyopathies. Various cardiac stress disorders, including dilated and hypertrophic cardiomyopathies, have been associated with the presence of soluble protein oligomers in cardiomyocytes (CMs) (1). Based on these findings, it has been suggested that protein misfolding and the ensuing proteo-

toxicity are important contributors to the establishment and progression of heart failure, and parallel cardiac dysfunction as a sort of Alzheimer's disease of the heart (2). Such information supports the idea that targeting the accumulation of misfolded proteins could be beneficial in patients with heart failure.

Several forms of systemic amyloidosis display congestive heart failure and a variety of alterations in cardiac electrogenesis and conduction that contribute considerably to disease-associated morbidity and mortality (3,4). Human transthyretin (TTR) is one of the proteins whose amyloid aggregates are often associated with heart disease. TTR is a 55 kD homotetramer that is synthesized by the liver and the choroid plexus, which carries T4 and the retinol-binding protein in the plasma and cerebrospinal fluid (5).

Submitted April 12, 2016, and accepted for publication September 6, 2016.

\*Correspondence: [monica.bucciantini@unifi.it](mailto:monica.bucciantini@unifi.it)

Laura Sartiani and Monica Bucciantini contributed equally to this work.

Editor: Michele Vendruscolo.

<http://dx.doi.org/10.1016/j.bpj.2016.09.010>

© 2016

Extracellular aggregates of wild-type TTR (wtTTR) are found in senile systemic amyloidosis (SSA), a condition that affects ~25% of the population over 80 years of age. A more severe phenotype characterizes familial amyloid cardiomyopathy (FAC), in which TTR aggregation occurs as a consequence of a number of described mutations in the TTR gene (6,7). Presently, an effective therapy against TTR amyloidosis is still lacking, and the most severe cases of SSA and FAC can be treated only by liver or heart transplantation. Correspondingly, the molecular and functional mechanisms underlying wtTTR aggregation and toxicity in cardiac tissue remain ill defined.

Amyloid aggregation of TTR is preceded by tetramer destabilization into monomers/dimers with an exposed hydrophobic surface and monomer/dimer misfolding, which results in structural reorganization into amyloid assemblies (8,9). Most of the known TTR mutations in humans have been shown to be amyloidogenic, favoring tetramer destabilization (10), whereas tetramer stabilization, which occurs in some mutants, such as the stable and nonamyloidogenic Thr119Met, as well as after T4 binding, slows down the rate of dissociation of the TTR tetramer, thus hindering fibril growth (11). Although numerous studies have addressed this issue in recent years, the identity of the cytotoxic species associated with amyloid disease and TTR amyloidosis is far from clear. Several studies indicated that fibril deposition into amyloid aggregates is usually preceded by the appearance of toxic, low-molecular-weight oligomeric aggregation nuclei (12,13) that impair cell viability, notably by altering intracellular ion homeostasis (14–16), although cell sufferance caused by a nutrient shortage due to the physical barrier posed by the fibrillar burden can play an important role as well (17). Accordingly, TTR fibrils, which were previously considered to be directly responsible for tissue impairment in familial amyloid polyneuropathy/FAC and SSA, are now thought to be far less toxic than their unstable oligomeric precursors, which are now considered to be mainly responsible for cell damage and tissue functional impairment (18). It has long been thought that the mass of deposited amyloid fibrils is solely responsible for tissue dysfunction; however, inflammation, apoptosis, and reactive oxygen species (ROS) markers characteristic of tissue damage can be detected in human carriers of mutant TTR well before the appearance of amyloid deposits. These markers have been associated with amorphous TTR aggregates that can be observed in the early stages of disease evolution (18). Nevertheless, a substantial body of experimental evidence fully demonstrates that amyloid fibrils are capable of causing cellular death in numerous situations (19–29). This raises the possibility that the molecular determinants underlying aggregate cytotoxicity are not always associated with the same type of species, and that there may well be oligomers and fibrils with different structural and biophysical properties, and hence with different abilities to interact

with, disassemble, permeabilize, and deregulate the cell membrane (30). Presently, very little information is available regarding the biochemical and cell modifications that occur in CMs exposed to aggregated TTR (31), whereas much is known about the biochemical alterations and specific functional (e.g., electrophysiological) abnormalities that result from exposure to toxic TTR amyloids of neuronal cells, with ensuing  $\text{Ca}^{2+}$  influx via TRPM8 and NaV1.8 channels (14). Furthermore, the possible involvement of specific lipid clusters in these modifications was inferred on the basis of some perturbation of  $\text{Ca}^{2+}$  conductance (15). Both mechanisms are potentially relevant for CMs.

In this study, we used HL-1 and primary mouse CM cultures exposed to aggregated wtTTR to investigate aggregate-cell interactions and the ensuing electrophysiological and biochemical modifications that result in cell functional and viability impairment. In particular, after performing a careful biophysical characterization of TTR aggregation in vitro, we investigated some electrophysiological alterations that occurred after cell exposure to TTR aggregates that recapitulate, in vitro, specific and crucial aspects of SSA. Our goal was to provide a complete picture of the cellular biochemical, functional, and viability impairments caused by wtTTR at different stages of aggregation. As far as we know, our findings are the first to be reported regarding the biochemical and electrophysiological modifications that occur in CMs exposed to amyloid aggregates of wtTTR. Our data provide novel, to our knowledge, insights into the molecular and functional basis of heart pathophysiology in TTR amyloidosis.

## MATERIALS AND METHODS

### wtTTR production

Recombinant wtTTR was produced in a bacterial expression system using the *Escherichia coli* BL21B DE3 (pLysS) strain. The expressed protein was purified by gel filtration and ion exchange chromatography, and its purity was checked with the use of agarose gel and SDS-PAGE. Native, T4-stabilized wtTTR (TTR-T4) was obtained by adding T4 to the wtTTR solution. Briefly, T4 was dissolved in DMSO (Sigma-Aldrich, St. Louis, MO) at a 1.0 mM concentration for 1 h at room temperature. The solution was then diluted in PBS containing wtTTR to a TTR-T4 ratio of 1:2. TTR oligomers (TTR-ol) and fibrils (TTR-fib) were generated by TTR incubation in 100 mM acetate buffer, pH 4.4, at 25°C for 24 h or 96 h, respectively. In all experiments, aggregate concentration was expressed as the soluble tetramer concentration.

### Congo Red assay and Fourier transform-infrared analysis

Fibril growth was followed via Congo Red (CR) assay and Fourier transform-infrared (FT-IR) analysis. The former was performed by mixing 133  $\mu\text{L}$  of the protein solutions with 867  $\mu\text{L}$  of a 10 mM phosphate buffer, pH 7.4, solution containing 20  $\mu\text{M}$  CR and 150 mM NaCl. Solutions without protein or without CR were also prepared as controls. The CR absorption spectra were acquired after 2–3 min of equilibration using an

Ultraspec 2000 spectrophotometer (Pharmacia Biotech, Scintec Instruments, Centerville, Virginia).

The FT-IR spectra were collected via attenuated total reflection on a protein-hydrated film using a standardized approach (32,33). Briefly, 3.0  $\mu\text{L}$  sample aliquots were deposited on the single reflection diamond plate of a Golden Gate attenuated total reflection device (Specac Kent, Orpington, UK) and the spectra were collected after the solvent evaporated. A 670-IR spectrometer (Varian Australia, Mulgrave, Australia) equipped with a nitrogen-cooled mercury cadmium telluride detector and an air dryer purging system was used under the following conditions: 2.0  $\text{cm}^{-1}$  spectral resolution, 25 kHz scan speed, 1000 scan coadditions, and triangular apodization. The second derivatives of the measured spectra were obtained by the Savitsky-Golay method using the Resolutions-Pro software (Varian Australia). The FT-IR spectrum of soluble TTR was collected at a 40  $\mu\text{M}$  protein concentration in 30 mM sodium phosphate buffer, pH 7.4. For aggregation studies, the TTR spectra were recorded at a 20  $\mu\text{M}$  protein concentration in 100 mM acetate buffer, pH 4.4.

### Dynamic light-scattering analysis

The size distributions of the protein samples by volume were obtained after sample centrifugation (18,000 rpm for 10 min). The data were obtained by means of a Zetasizer Nano S dynamic light-scattering (DLS) device (Malvern Instruments, Worcestershire, UK) using low-volume disposable cells (12.5  $\times$  45 mm). The temperature was maintained at 25°C by a thermostated system. The acetate buffer was filtered immediately before use to clean off any impurity.

### Atomic force microscopy and transmission electron microscopy analyses of TTR aggregates

For atomic force microscopy (AFM), a 10  $\mu\text{L}$  aliquot of the sample was deposited on a freshly cleaved mica substrate and dried under mild vacuum. The AFM images were acquired in tapping mode in air using a Dimension 3100 SPM equipped with a G scanning head (maximum scan size 100  $\mu\text{m}$ ) and driven by a Nanoscope IIIa controller, or a Multi-mode SPM equipped with an E scanning head (maximum scan size 10  $\mu\text{m}$ ) driven by a Nanoscope IV controller (Digital Instruments, Bruker, Karlsruhe, Germany). Single-beam, uncoated silicon cantilevers (type OMCL-AC160TS; Olympus, Tokyo, Japan) were used. The drive frequency was in the 290–330 kHz range and the scan rate was in the 0.5–1.0 Hz range.

For transmission electron microscopy (TEM) analysis, sample aliquots were withdrawn from the aggregation mixture at regular time intervals to monitor the assembly process after adsorption onto formvar/carbon-coated 400 mesh nickel grids (Agar Scientific, Stansted, United Kingdom) and negative staining with 2.0% (w/v) uranyl acetate (Sigma-Aldrich). The grids were observed at a 15–30,000 $\times$  magnification in a JEM (LabWrench, Ontario, Canada) 1010 transmission electron microscope with an 80 kV excitation voltage.

### Dot-blot assay

For the dot-blot assay, 5.0  $\mu\text{L}$  samples of 10  $\mu\text{M}$  wtTTR were spotted onto a nitrocellulose membrane and left to dry. Then the membrane was blocked with 3.0% bovine serum albumin, 0.1% Tween-20 in TBS (50 mM Tris-HCl buffer, pH 7.5, 150 mM NaCl) for 1.0 h at room temperature, and incubated overnight at 4°C with rabbit anti-TTR polyclonal antibodies (1:2000) and with conformation-specific antibodies (rabbit anti-oligomer (A11; 1:10000) or rabbit anti-fibril (OC; 1:5000) polyclonal antibody). After three washes in TBS/0.1% Tween-20, the membrane was incubated for 1.0 h at room temperature with peroxidase-conjugated anti-rabbit or anti-mouse antibodies (1:10,000). After three washes in TBS/0.5% Tween-20, immuno-

detection was performed using the SuperSignal West Pico chemiluminescent substrate (Thermo Fisher Scientific, Waltham, MA) and Kodak Biomax MS film (Sigma-Aldrich, Saint Louis, Missouri).

### HL-1 CM and human dermal fibroblast $\alpha$ cell culture

HL-1 CMs were obtained from Dr. W.C. Claycomb (Louisiana State University) and grown in T25, gelatin/fibronectin-coated flasks as previously described (34). The cells were maintained in Claycomb medium (JRH Biosciences, Sigma-Aldrich, Saint Louis, Missouri) supplemented with 10% fetal bovine serum (Life Technologies, Monza, Italy), 2.0 mM L-glutamine (Life Technologies), 0.1 mM noradrenaline (Sigma-Aldrich), and 100 units/mL penicillin-streptomycin (Life Technologies). At confluence, the cells were detached and replated at a 1:3 dilution in a new T25 flask or in 96-well plates and used for experimental measurements. Human dermal fibroblast  $\alpha$  (HDF $\alpha$ ) cells were cultured at 37°C in complete medium (Dulbecco's modified Eagle's medium (DMEM), 10% fetal bovine serum, 3.0 mM glutamine, 100 units/mL penicillin and 100  $\mu\text{g}/\text{mL}$  streptomycin) in a humidified, 5.0%  $\text{CO}_2$  incubator. Every 3 days, the cells (70–90% confluent) were detached and replated at a 1:3 dilution in a new plate or in 96-well plates and used for measurements.

### Isolation of mouse ventricular myocytes

Left ventricular CMs were isolated from adult C57/6BL mice (Charles River, Wilmington, MA) by enzymatic digestion. Briefly, after heparin injection (5000 units/mL) and anesthesia with isoflurane, the heart was rapidly excised, mounted on a Langendorff apparatus, and perfused with perfusion buffer (see solutions) prewarmed at 37°C and equilibrated with 100%  $\text{O}_2$ . Then, the solution was quickly changed to perfusion buffer plus Liberase DL (0.05 mg/mL; Roche Diagnostics, Indianapolis, IN) and  $\text{CaCl}_2$  (12.5  $\mu\text{M}$ ). The left ventricle was excised, minced, and stirred in perfusion buffer containing  $\text{CaCl}_2$  (12.5  $\mu\text{M}$ ) and bovine serum albumin (1.0 mg/mL; Sigma-Aldrich). The CMs were collected by gravity sedimentation and stored in Tyrode's solution containing 0.5 mM  $\text{CaCl}_2$  and 4.0% penicillin-streptomycin solution at room temperature. All recordings were completed within 4–6 h from the time of cell isolation.

### Calcium imaging

Intracellular  $\text{Ca}^{2+}$  handling was evaluated as previously described (35). Briefly, HL-1 and mice ventricular CMs were incubated for 20 min at 37°C in Tyrode's solution containing 1–5  $\mu\text{L}/\text{L}$  fluo-3-acetoxymethyl ester (FLUO-3 AM; Molecular Probes, Eugene, OR) and 1.0  $\mu\text{L}/\text{mL}$  Pluronic F127 solution (Molecular Probes) for dye loading. The preparation was set in the stage of a fluorescence microscope (DMIRE2; Leica, Mannheim, Germany) properly equipped for fluorescence signal production and detection. Fluo-3 was excited with the light of a xenon lamp (LPS 220; Photo Technology International, HORIBA UK, Middlesex, UK), using a bandpass filter set at  $480 \pm 15$  nm. Fluo-3 fluorescence was detected at  $540 \pm 15$  nm.  $\text{Ca}^{2+}$  release from sarcoplasmic reticulum (SR) stores was studied using 5.0  $\mu\text{M}$  ryanodine (Rya; Tocris Bioscience, Ellisville, MO) or 5.0  $\mu\text{M}$  2-aminoethyl diphenylborinate (2-APB; Sigma-Aldrich) to block the Rya and IP3 receptors, respectively. CMs were preincubated with the inhibitors for 15 min before recordings were obtained. Experimental control of fluorescence acquisition was performed using the software Imaging Workbench (INDEC BioSystems, Santa Clara, California). Data analysis was carried out using the Axon Imaging Workbench program (v2.2.1; Axon Instruments, Foster City, California) or Metafluor (Molecular Devices, Sunnyvale, CA).  $\text{Ca}^{2+}$  cumulative content was evaluated in HL-1 CMs as the integrated area under the curve after 20 min of exposure to experimental conditions and reported as the mean fractional variation (mean  $\pm$  SE)

with respect to the vehicle. Ventricular CMs were paced at 1.0 Hz 1–5 V (pulse duration 1.0 ms) and the  $\text{Ca}^{2+}$  transients were analyzed to calculate the amplitude, baseline level, time to peak, and 50% and 90% decay times. The data were reported as mean fractional variation (mean  $\pm$  SE) relative to the initial values measured for individual cells.

## Patch-clamp recordings

Electrophysiological recordings were performed as previously described (36). The cells were placed in a thermostatic bath on the platform of an inverted microscope (Diaphot TMD; Nikon, Kawasaki, Japan). The patch-clamped cell was superfused by means of a temperature-controlled ( $36 \pm 0.5^\circ\text{C}$ ) microsyringe, allowing rapid changes of the cell-bathing solution. Action potentials were recorded using a patch amplifier (Axopatch 200B; Molecular Devices) in whole-cell configuration (current clamp mode) at 1.0 Hz and the signals were digitized via a DAC-ADC interface (Digidata 1200B; Molecular Devices) acquired by means of pClamp software (version 10; Molecular Devices), and analyzed using Origin 7.5 (GraphPad Software). The patch-clamp pipettes, prepared from glass capillary tubes (borosilicate GC150T; Harvard Apparatus, Saint Laurent, Canada) by means of a two-stage puller (P-97; Sutter Instrument, Novato, CA), displayed a resistance of 3.5–5.0 M $\Omega$  when filled with the internal solution. During the patch-clamp experiments, TTR aggregates were added to the internal pipette solutions.

The following solutions were used for calcium imaging and electrophysiology:

- Perfusion buffer (mM): NaCl 113, KCl 4.7,  $\text{KH}_2\text{PO}_4$  0.6,  $\text{Na}_2\text{PO}_4$  0.6,  $\text{MgSO}_4$  1.2,  $\text{NaHCO}_3$  12,  $\text{KHCO}_3$  10, HEPES 10, taurine 30, BDM 10, D-(+)-glucose 10, pH 7.30.
- Tyrode's solution (mM): D-(+)-glucose 10, Hepes 5.0, NaCl 140, KCl 5.4,  $\text{MgCl}_2$  1.2,  $\text{CaCl}_2$  0.0125, pH 7.3.
- Pipette solution (mM): K-aspartate 130,  $\text{Na}_2\text{-ATP}$  5,  $\text{MgCl}_2$  2.0,  $\text{CaCl}_2$  5.0, EGTA 11, HEPES-KOH 10, pH 7.2.

## ROS measurement

Intracellular ROS levels were determined using the fluorescent probe 2',7'-dichlorofluorescein diacetate, acetyl ester (CM-H<sub>2</sub> DCFDA; Thermo Fisher Scientific/Molecular Probes). CM-H<sub>2</sub> DCFDA is a cell-permeant indicator for ROS that becomes fluorescent upon removal of the acetate groups by intracellular esterases and subsequent oxidation. The latter modification can be detected by monitoring the increase in fluorescence at 538 nm. The HL-1 cells were plated at a density of 10,000 cells per well on 96-well plates. After 24 h of cell exposure to the aggregates (10  $\mu\text{M}$  TTR monomer concentration), 10  $\mu\text{M}$  DCFDA in DMEM without phenol red was added. After 30 min, the fluorescence values at 538 nm were detected with the use of a Fluoroskan Ascent FL (Thermo Fisher Scientific/Molecular Probes).

## Cell viability assay

The cytotoxicity of the different forms of soluble or aggregated TTR was assessed via a 3-(4,5-dimethylthiazol-2-yl)-2,5-diphenyltetrazolium bromide (MTT) reduction inhibition assay. Briefly, the cells were plated at a density of 1500 cells/well on 96-well plates in 100  $\mu\text{L}$  of culture medium. After 48 h, the medium was changed with 100  $\mu\text{L}$  of fresh medium containing the different TTR aggregates (10  $\mu\text{M}$  monomer concentration) or with an equal volume of aggregation buffer (control cells). After 24 h, the cells were incubated for 2.0 h with 100  $\mu\text{L}$  of serum-free DMEM without phenol red, containing 0.5 mg/mL MTT. Finally, 100  $\mu\text{L}$  of cell lysis solution (20% SDS, 50% N,N-dimethylformamide) was added to each well. After sample incubation at 37°C to allow complete lysis, the blue formazan

absorbance was read at 570 nm with an automatic plate reader (Bio-Rad, Life Science, Segrate, Italy). Cell apoptosis was detected by using the Annexin V-FITC apoptosis detection kit (Sigma-Aldrich). A propidium iodide (PI) solution with Annexin V-FITC was used to discriminate among viable, apoptotic, and secondary necrotic cells. Briefly, after a 24 h treatment with the TTR aggregates, the cells were incubated with Annexin V-FITC and PI for 10 min at room temperature. The cells were then analyzed by flow cytometry, and cell viability was determined using the Trypan Blue exclusion method. HL-1 cells were treated with TTR aggregates, and after 24 h they were centrifuged at  $200 \times g$  and incubated in 0.2% Trypan Blue (Sigma-Aldrich) for 10 min at 37°C. The cells were then washed in PBS and counted via phase-contrast microscopy. In this assay, blue cells were considered to have lost membrane integrity and were scored as nonviable. All counts were performed in triplicate.

## Sialic acid cleavage and quantification

The sialic acid moiety was removed from gangliosides as previously described (37). Briefly, the cells were starved by incubation with DMEM serum-free media for 3.0 h at 37°C and then left standing for 2 h in the presence of a mixture of neuraminidases (NAM) from *Vibrio cholerae* (11.7 mU) and *Clostridium perfringens* (100 mU; Sigma-Aldrich). The removed sialic acid was measured enzymatically using a specific kit (Roche Molecular Biochemicals, Mannheim, Germany) according to the manufacturer's instructions.

## Mitochondrial membrane potential in living cells

Changes in the mitochondrial membrane potential ( $\Delta\Psi_M$ ) in TTR-exposed cells (10  $\mu\text{M}$  TTR monomer concentration) were detected by a fluorescence-based assay. The cells were cultured for 10 min at 37°C on coverslips in DMEM containing 5.0 mg/mL of the lipophilic cationic probe (fluorochrome(5,5,6,6-tetrachloro-1,1,3,3-tetraethylbenzimidazolcarbocyanine iodide) (JC-1 stain; Thermo Fisher Scientific). At a hyperpolarized mitochondrial membrane potential (–140 mV), this dye forms a red fluorescent J-aggregate, whereas at a depolarized membrane potential (–100 mV) it remains in the green fluorescent monomeric form. Before detection, the cells were washed in PBS and placed in an open slide-flow loading chamber mounted on the stage of a confocal scanning microscope (Bio-Rad) equipped with a krypton/argon laser source. The emitted fluorescence was monitored at 488 nm and 568 nm with a Nikon plan ApoX60 oil-immersion objective. Series of optical sections ( $512 \times 512$  pixels) were taken through the depth of the cells with a thickness of 1.0  $\mu\text{m}$  at intervals of 0.8  $\mu\text{m}$ . Twenty optical sections for each sample were projected as a single composite image by superimposition.

## Confocal immunofluorescence

Subconfluent HL-1 cells grown on glass coverslips were exposed to 10  $\mu\text{M}$  TTR aggregates (monomer concentration) for 24 h. After incubation, the cells were washed with PBS and fixed in 2.0% buffered paraformaldehyde for 10 min. Then, the cells were counterstained with 50  $\mu\text{g}/\text{mL}$  tetramethylrhodamine-conjugated wheat germ agglutinin (Thermo Fisher Scientific/Molecular Probes) for 45 min at room temperature, permeabilized by treatment with acetone at  $-20^\circ\text{C}$  for 1.0 min, washed with PBS, and blocked with PBS containing 0.5% bovine serum albumin and 0.2% gelatin. After counterstaining, the cells were incubated for 1.0 h at room temperature with an anti-TTR rabbit polyclonal antibody or with an anti-oligomer rabbit polyclonal antibody (A11) diluted to 1:1000 and 1:10,000, respectively, in the blocking solution and then washed with PBS for 30 min under stirring. The immune reaction was revealed by Alexa488 or Alexa568-conjugated anti-rabbit secondary antibody (Thermo Fisher Scientific/Molecular Probes) diluted 1:400 in PBS. Finally, the cells were

washed twice in PBS and once in redistilled water to remove any nonspecifically bound antibody.

Cell-surface monosialotetrahexosylganglioside (GM1) labeling was performed by incubating the cells with 10 ng/mL Alexa488-conjugated cholera toxin B (CTX-B) in complete medium for 20 min at room temperature. Cell fluorescence was imaged using a confocal TCS SP5 scanning microscope (Leica) equipped with a HeNe/Ar laser source for fluorescence measurements. The observations were performed using a Leica Plan Apo X63 oil immersion objective, suited with optics for differential interference contrast acquisition. Series of 0.5- $\mu$ m-thick optical sections ( $1024 \times 1024$  pixels) were taken through the cell depth at 0.4  $\mu$ m intervals and 20 optical sections for each examined sample were Z projected. To quantify the immunofluorescence intensity of cell-associated TTR, we randomly selected 10 fields of view from three separate experiments. Colocalization analysis was performed by using developed algorithms such as Mander's overlap coefficient and the colocalization coefficients  $k_1$  and  $k_2$  (38):

$$R = \frac{\sum_i S1_i \cdot S2_i}{\sqrt{\sum_i (S1_i)^2 \cdot \sum_i (S2_i)^2}}$$

$$k_1 = \frac{\sum_i S1_i \cdot S2_i}{\sum_i (S1_i)^2} \quad k_2 = \frac{\sum_i S1_i \cdot S2_i}{\sum_i (S2_i)^2},$$

where  $S1$  and  $S2$  represent the signal intensity of pixels in channels 1 and 2, respectively.

## Data analysis and statistics

Statistical analysis was performed by means of the Prism program (GraphPad software), using Student's  $t$ -test for grouped data or analysis of variance (ANOVA) followed by Tukey's multiple-comparisons test for all other values. A  $p$ -value of  $<0.05$  was considered significant.

## RESULTS

### Morphological analysis and biophysical properties of wtTTR aggregates

The wtTTR assemblies TTR-T4, TTR-ol, and TTR-fib, grown at pH 4.4 for different incubation times, were first characterized by spectroscopic and morphological analyses. The conformational properties of TTR-T4 and aggregated TTR were initially investigated at pH 7.4 by FT-IR spectroscopy, which allows one to study protein secondary structure and aggregation by analyzing the IR absorption spectrum in the Amide I region ( $1700$ – $1600$   $\text{cm}^{-1}$ ). TTR-T4 displayed the Amide I maximum around  $1630$   $\text{cm}^{-1}$  (Fig. 1 A), a signal that resulted from the intramolecular  $\beta$ -sheet structure of the native protein (28). The second derivative of the spectrum (Fig. 1 B) revealed additional components at  $\sim 1691$   $\text{cm}^{-1}$ ,  $\sim 1675$   $\text{cm}^{-1}$ , and  $\sim 1649$   $\text{cm}^{-1}$ , which could be assigned to  $\beta$ -sheets, turns/ $\beta$ -sheets, and  $\alpha$ -helical/random coil structures, respectively. At pH 4.4, the wtTTR fibrillized. Under these conditions, after  $\sim 3$  min the peak at  $1630$   $\text{cm}^{-1}$  assigned to the intramolecular  $\beta$ -sheet component slightly decreased in intensity and shifted to higher wave numbers (Fig. 1, A and B), suggest-

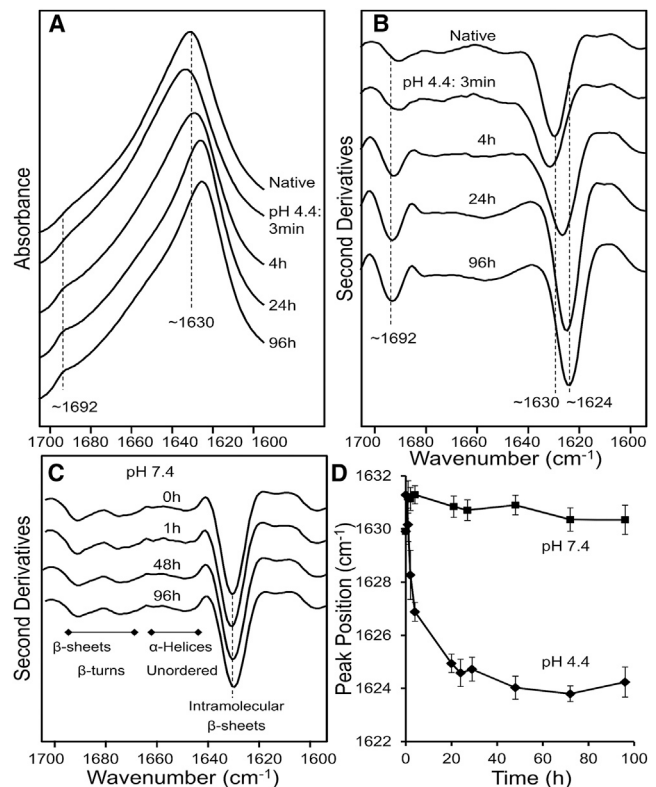


FIGURE 1 Characterization of wtTTR by FT-IR. (A) FT-IR absorption spectra of native TTR and of TTR incubated at pH 4.4 for different time lengths. (B) Second derivatives of the absorption spectra reported in (A). (C) Second derivatives of the absorption spectra of TTR incubated at pH 7.4 for different lengths of time. The peak positions of the main components are also given. The spectra are reported after normalization to the Amide I band area. (D) Peak positions (taken from the second derivative spectra) of the main  $\beta$ -sheet component reported versus incubation time at pH 7.4 or pH 4.4.

ing partial unfolding/misfolding of the TTR secondary structures, as previously reported for other proteins (32,39). Prolonged incubation at pH 4.4 resulted in the appearance of a downshift of the main  $\beta$ -sheet component, indicating some rearrangement of the  $\beta$ -sheet contacts in the growing aggregates. After 96 h of incubation, the TTR spectrum displayed both a narrower Amide I band (as compared with that of the natively folded protein, whose maximum downshifted to  $\sim 1624$   $\text{cm}^{-1}$ ) and a new, well-resolved component at  $\sim 1692$   $\text{cm}^{-1}$ , characteristic of intermolecular  $\beta$ -sheets in amyloid fibrils (40,41). These modifications of the FT-IR spectra of wtTTR were not found at pH 7.4, where the spectra collected at different times of incubation were almost superimposable with that obtained at  $T_0$  without any apparent changes (Fig. 1 C), indicating protein stability. The different behaviors of wtTTR at pH 4.4 and pH 7.4 were more evident when the peak position of the main  $\beta$ -sheet component was plotted against time (Fig. 1 D), since the plot was sharply modified only at the acidic pH.

In the first 24 h of TTR incubation at pH 4.4, AFM and TEM imaging (Fig. 2, A and B) showed the presence of different-sized oligomeric structures (TTR-ol,  $2.7 \pm 0.1$  nm high) coexisting with short, worm-like prefibrillar assemblies ( $3.5 \pm 0.1$  nm high). These protofibrils displayed a nodular morphology, resembling short chains of beads. Amyloid fibrils (TTR-fib) were not present at this aggregation time. Fibrils  $5.7 \pm 0.1$  nm in height appeared later, after 96 h of protein incubation.

The transition from natively folded to oligomeric TTR was also investigated via DLS. An apparent hydrodynamic diameter ( $D_{h,app}$ ) of  $\sim 7.0$  nm was found for TTR-T4, which was consistent with its tetrameric structure (Fig. 2 E) (42). However, after wtTTR incubation for 24 h at acidic pH, larger oligomeric forms with a  $D_{h,app}$  of  $\sim 1000$  nm appeared, and became prevalent with increasing time (Fig. 2 E).

To further investigate the nature of the oligomeric and fibrillar structures grown under these conditions, we analyzed the aggregated TTR samples by immunoblotting using the oligomer-specific A11 antibody and the fibril-specific OC antibody. The A11 antibody immunostained both the TTR-ol and, to a lesser extent, TTR-fib samples, but only TTR-fib showed a significant OC immunoreactivity. In contrast, TTR-T4 did not exhibit any immunoreactivity with either the A11 or OC antibody (Fig. 2 C). The amyloid nature of TTR-ol and TTR-fib was further confirmed by the red shift of the CR absorbance maximum, a signature of the amyloid fold (Fig. 2 D). The shift was not observed in the TTR-T4 incubated under the same conditions (data not shown).

## Immunolocalization of TTR aggregates

After having described the structural features of TTR, both natively folded (TTR-T4) and under aggregating conditions (TTR-ol, TTR-fib), we sought to determine whether these different TTR species were able to interact with the plasma membrane of cultured HL-1 cells, and if so, the extent of the interaction. When the cells were exposed to the stabilized TTR-T4, we failed to detect any protein interaction with the cell membrane (Fig. 3 A), in agreement with recently reported data relative to the nonamyloidogenic, stabilized T119M variant (31). However, a significant association of TTR aggregates with the cell surface was seen in HL-1 cells treated with TTR-ol or TTR-fib (Fig. 3, B and C). Contrary to the case with TTR-fib, TTR-ol was found to be significantly internalized into these cells after 24 h of exposure, as shown by a representative magnified Y projection of a cell: TTR-fib was only observed in contact with the outer surface of the cell membrane (Fig. 3 E), whereas TTR-ol was found in the cytoplasm as A11-immunopositive punctate fluorescence (Fig. 3 D). The association of oligomers and fibrils with the cell membrane was also evident (to a less extent for the fibril sample) on HDF $\alpha$ , as shown in Fig. S1 in the Supporting Material, suggesting that TTR aggregates did not exhibit a distinct cellular specificity. However, no internalization of oligomeric species was evident in these cells (Fig. S1).

The role of the monosialoganglioside GM1, a major raft marker, in promoting aggregate-membrane interaction was

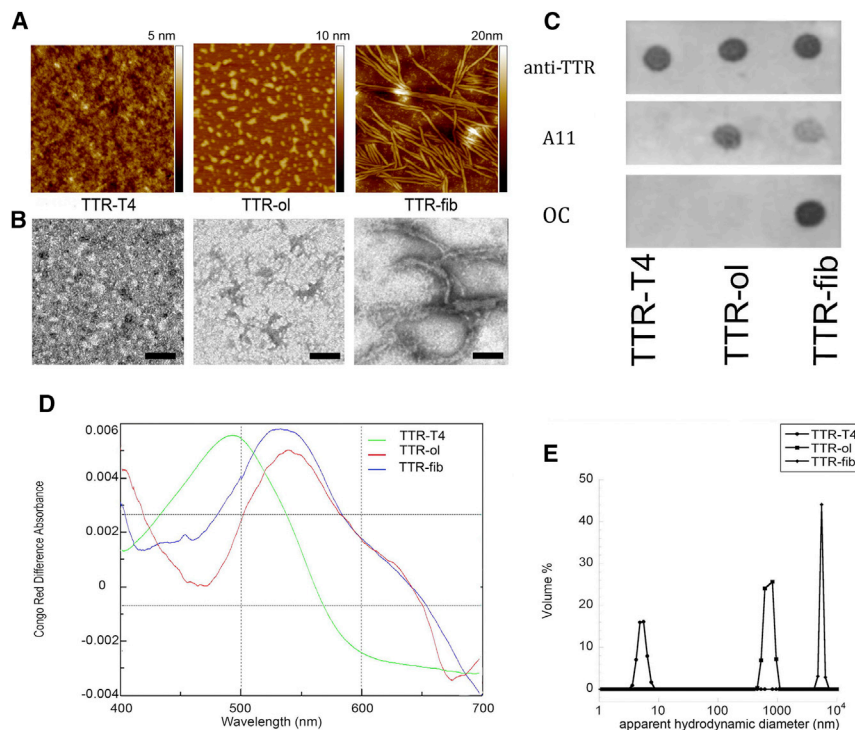
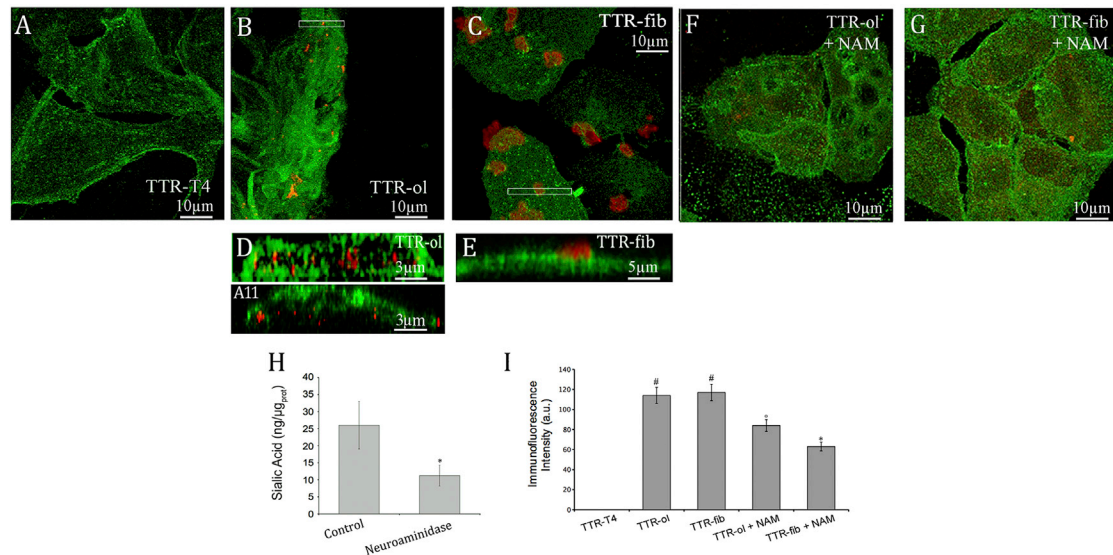


FIGURE 2 Morphological characterization of TTR aggregates. (A) AFM images of TTR-T4, TTR-ol, and TTR-fib. Scan size,  $1.0 \mu\text{m}$ . (B) TEM images of TTR-T4, TTR-ol, and TTR-fib (scale bar, 200 nm). (C) Dot blotting of TTR-T4, TTR-ol, and TTR-fib using anticonformational A11 and OC antibodies. Three replicates were generated and probed separately by anti-TTR, A11, and OC antibody. (D) CR absorption spectra of TTR-T4 (green line), TTR-ol (red line), and TTR-fib (blue line). (E) DLS analysis of TTR-T4, TTR-ol, and TTR-fib, showing the volume distribution of the particle apparent hydrodynamic diameter. To see this figure in color, go online.



**FIGURE 3** Confocal analysis. (A–C) Confocal images of HL-1 cells treated with wtTTR. The cells were exposed for 24 h to 10 μM (A) TTR-T4, (B) TTR-ol, and (C) TTR-fib. (D and E) Z projections. (F and G) HL-1 cells were pretreated with NAM to reduce sialic acid on the cell surface and incubated for 24 h with 10 μM TTR-ol (F) and TTR-fib (G). The cells were stained with cholera toxin (green) and then were fixed, permeabilized, and stained with anti-TTR antibody (red) or A11 antibody (red). (H) Sialic acid quantification. HL-1 cells were treated with 11.7 mUI of *V. cholera* neuraminidase and 5.0 mUI of *Arthrobacter ureafaciens* neuraminidase for 1.0 h at 37°C in serum-free medium. The sialic acid levels in the membrane fractions were analyzed enzymatically with the use of a sialic acid quantification kit; \* $p < 0.05$ . (I) Quantitative analysis of TTR binding on the cells. Each graph displays the mean values  $\pm$  SE and a statistical comparison between TTR-T4-treated cells and cells treated as indicated ( $n = 5$ ; \* $p < 0.05$ ,  $^{\circ}p < 0.01$ , # $p < 0.001$ ). To see this figure in color, go online.

also investigated. In fact, recent data indicate that besides favoring peptide/protein misfolding and aggregation, GM1 can also mediate the interaction of amyloid assemblies with the plasma membrane, notably by means of its negatively charged sialic acid component (27). Therefore, to further elucidate whether our TTR aggregates interacted with the cell membrane at GM1-rich sites, as well as the role of the negatively charged sialic acid moiety of GM1, we carried out confocal fluorescence microscopy experiments using a polyclonal antibody raised against wtTTR. The cell membrane was counterstained by Alexa 488-conjugated CTX-B, a fluorescent probe that binds predominantly GM1 on the cell membrane. In some experiments, the cells were treated with a mixture of NAM to specifically cleave sialic acid residues from the cell surface before aggregate exposure. For reducing membrane GM1, this treatment is milder than treating cells with fumonisin or other inhibitors of GM1 synthesis because it maintains the GM1 backbone inside the bilayer and therefore does not perturb the membrane lipid order. The treatment caused a significant decline (~2.5-fold) of the sialic acid on HL-1 cells, as shown in Fig. 3 H, without affecting cell viability (data not shown). Under these conditions, we found that the signals of both TTR-ol and TTR-fib on the cell membrane were significantly reduced in NAM-treated cells (Fig. 3, F, G, and I). The colocalization analysis using the overlap coefficient did not show significant differences between NAM-treated and -untreated samples (Table 1). Therefore, the ratio between the overlap coefficients  $k_1$  (weighted overlap of

TTR immunofluorescence (red) to GM1 fluorescence) and  $k_2$  (weighted overlap of GM1 fluorescence (green) to TTR immunofluorescence) was used to determine the degree of GM1 recruitment in the colocalization areas (42). The analysis showed that the  $k_1/k_2$  ratio was lower in the cells treated with TTR-fib than in those treated with TTR-ol, suggesting that TTR fibrils promote higher GM1 recruitment in the colocalization areas. When the cells were treated with NAM, the  $k_1/k_2$  ratio increased but the total TTR immunofluorescence signal decreased, as shown in Fig. 3 I, indicating that in NAM-treated cells, fibril-membrane interactions and GM1 clustering on the cell membrane were reduced.

Aggregate recruitment to the cell membrane was deeply dependent on the presence of negatively charged molecules, notably GM1, whose decrease affected fibril binding much more than oligomer binding.

Taken together, these data confirm that TTR aggregates bind at the cell surface, thus favoring oligomer internalization. They also suggest that the interaction involves GM1 and occurs preferentially at its negatively charged moiety, highlighting the importance of electrostatic binding. Finally, our data agree with previous studies indicating that TTR

**TABLE 1** Colocalization Analysis of TTR Oligomers/Fibrils and GM1 on the Plasma Membrane of HL-1 Cardiomyocytes

	TTR-ol	TTR-fib	TTR-ol + NAM	TTR-fib + NAM
Overlap coefficient	0.895	0.899	0.839	0.850
$k_1/k_2$	0.855	0.448	3.070	2.56

aggregates have a high affinity for synthetic lipid membranes rich in anionic phospholipids (43).

### Aggregate cytotoxicity

Once we established that different wtTTR aggregates bind to membrane sites where sialic acid residues, notably those bound to GM1, are present, and that binding is followed by internalization in the case of oligomers, we tested whether such events modulate cell viability and cause distinct biological effects. Initially, we checked TTR cytotoxicity to HL-1 cells by performing an MTT reduction assay. As expected, TTR-T4 was harmless to exposed cells (Fig. 4 A), in similarity to the stabilized T119M mutant (31), whereas TTR-ol and TTR-fib displayed significant cytotoxicity, in agreement with their ability to interact with the plasma membrane (Fig. 4 A). We also assessed the cytotoxic effect of TTR aggregates on HDF $\alpha$  cells. These cells, despite the presence of aggregate on the membrane, were more resistant to amyloid insult (Fig. S1), suggesting that various cell types exposed to the same toxic aggregates have different vulnerabilities. The decreased MTT reduction observed in HL-1 cells was not related to apoptotic or necrotic events (data not shown), suggesting that after 24 h of exposure to TTR aggregates, the HL-1 cells showed a significant impairment of mitochondrial functionality without cell death or activation of apoptosis. This finding was confirmed by the ROS-sensitive fluorescent probe CM-H<sub>2</sub> DCFDA; in fact, we found that incubation for 24 h with TTR-ol stimulated ROS production in HL-1 cells and that this effect was enhanced when the cells were exposed to TTR-fib (Fig. 4 B). We used the JC-1 dye to further investigate whether aggregate cytotoxicity is associated with mitochondrial dysfunction, as was previously shown for A $\beta$  aggregates in Alzheimer's disease (44). For this purpose, we used confocal microscopy to assess the effect on the mitochondrial membrane potential ( $\Delta\psi_m$ ) of HL-1 exposure to TTR-T4 or to variously aged wtTTR aggregates. We found a significant yet similar decrease of  $\Delta\psi_m$  in cells exposed to

TTR-ol or TTR-fib, but not to TTR-T4 (Fig. 4, C and D), as shown by the disappearance of red fluorescence and/or the increase of green fluorescence. In particular, some cells were devoid of red fluorescence, which indicates the loss of  $\Delta\psi_m$  and the severity of the cell damage. These data indicate that in HL-1 cells, the cytotoxicity of extracellular TTR oligomers and fibrils proceeds through adsorption to the plasma membrane and results in ROS generation and alteration of the mitochondrial membrane potential.

### Effect of TTR aggregates on cytoplasmic calcium levels in HL-1 CMs

It was previously reported that both Ca<sup>2+</sup> deregulation and endoplasmic reticulum stress contribute to TTR toxicity to neuronal cells (15,16). We therefore investigated whether some acute deregulation of cytoplasmic Ca<sup>2+</sup> levels contributed to early events after the interaction of aggregated wtTTR with the sarcolemma and subsequent oligomer internalization. Typical experimental traces detected in quiescent HL-1 cells (i.e., not exhibiting spontaneous action potentials and associated intracellular Ca<sup>2+</sup> oscillations) are reported in Fig. 5 A, which shows a slow, progressive increase of Ca<sup>2+</sup> levels during acute cell exposure to the same concentration of either TTR-ol (gray trace) or TTR-fib (black trace). Under all conditions, the Ca<sup>2+</sup> concentration was sensitive to caffeine, which, as expected, evoked a fast, transient Ca<sup>2+</sup> increase after the depletion of SR stores. The cumulative Ca<sup>2+</sup> content was calculated as the integrated area under the curve recorded for 20 min and expressed as the fractional variation (mean  $\pm$  SE; Fig. 5 B) relative to the vehicle. The Ca<sup>2+</sup> increase was statistically significant with respect to the vehicle for both TTR-ol and TTR-fib, but not for TTR-T4 (see Table S1 for a detailed statistical analysis).

Spontaneous calcium oscillations were observed in nearly one-third of confluent HL-1 cells exposed to vehicle at 37°C (Fig. 6 A), and as previously reported (44,45), oscillations appeared irregular in frequency, amplitude, and duration

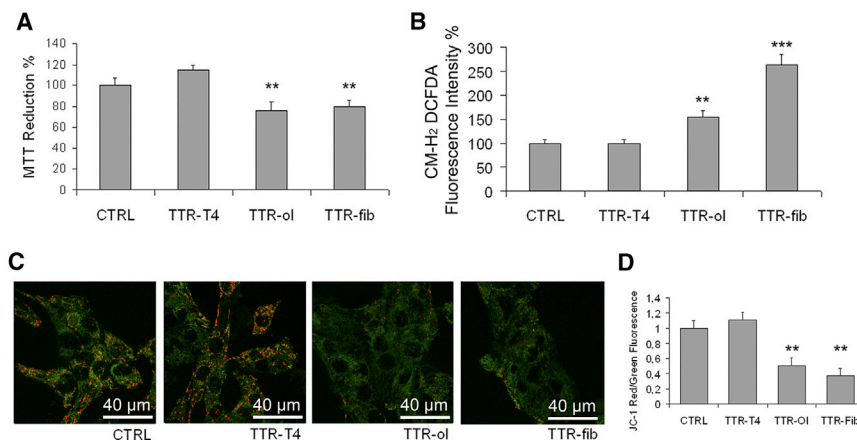
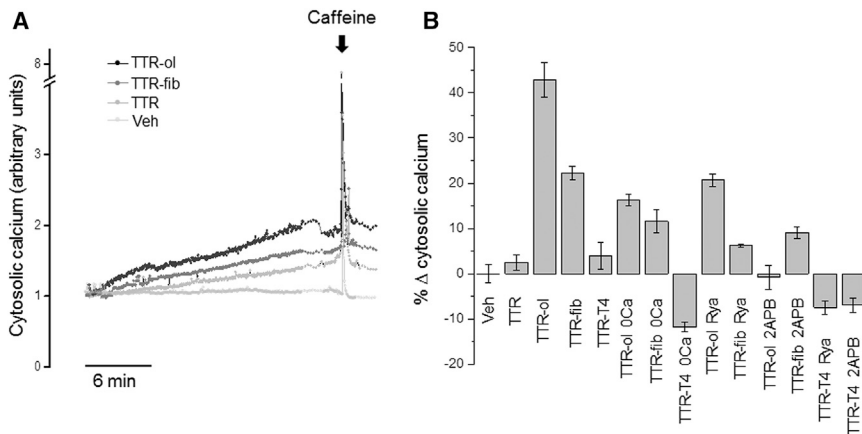


FIGURE 4 Cell viability, ROS levels, and mitochondrial dysfunction. (A–C) Cytotoxicity of TTR-T4, TTR-ol, and TTR-fib to human HL-1 cells as determined by MTT reduction assay (A), intracellular ROS production (B), and JC-1 assay (C). (D) Quantification of  $\Delta\psi_m$  expressed as a ratio (J-aggregates/monomer) in the different treatment groups. The values shown are normalized against the buffer control ( $n = 3$ , mean  $\pm$  SD). The statistics were analyzed by unpaired Student's  $t$ -test (\*\* $p < 0.01$ , \*\*\* $p < 0.001$ ). To see this figure in color, go online.



**FIGURE 5** Effects of different TTR samples on cytoplasmic calcium levels in HL-1 CMs. (A) Time course of cytosolic  $\text{Ca}^{2+}$  signals detected in HL-1 CMs exposed to  $10 \mu\text{M}$  TTR-ol or TTR-fib (monomer concentration) for 20 min before SR depletion with 10 mM caffeine. (B) Mean fractional variation ( $\pm$  standard error of the mean) relative to vehicle of cumulative cytosolic  $\text{Ca}^{2+}$  calculated after 20 min of exposure to different experimental conditions. Abbreviations: Veh, vehicle; TTR-ol, oligomeric transthyretin; TTR-fib, fibrillar transthyretin; TTR-T4, native TTR complex with thyroid hormone; TTR-ol 0 Ca, oligomeric TTR in  $\text{Ca}^{2+}$ -free medium; TTR-fib 0 Ca, fibrillar TTR in  $\text{Ca}^{2+}$ -free medium; TTR-ol Rya, oligomeric TTR plus ryanodine; TTR-ol 2-APB, oligomeric TTR plus 2-APB; TTR-fib Rya, fibrillar TTR plus ryanodine; TTR-fib 2-APB, fibrillar TTR plus 2-APB. The statistical analysis (ANOVA followed by Tukey's multiple-comparisons test) is reported in [Table S1](#).

(see inset of [Fig. 6 A](#)). The estimated oscillation frequency values were  $6.3 \pm 1.1$  beats per minute (bpm) for cells treated with vehicle ( $n = 19$ ),  $5.4 \pm 2.5$  bpm for cells treated with wtTTR ( $n = 14$ ), and  $5.9 \pm 1.5$  bpm for cells treated with TTR-T4 ( $n = 15$ ). Notably, the baseline calcium signal remained constant throughout the experimental interval with the vehicle as well as with wtTTR or TTR-T4 ([Fig. 6, B and K](#)). Interestingly, neither TTR-fib nor TTR-ol produced any gross modification in the oscillation frequency values ( $6.3 \pm 1.2$  bpm ( $n = 11$ ) and  $5.6 \pm 1.5$  bpm ( $n = 17$ ), respectively); however, similar to what was observed for quiescent HL-1 cells, both TTR-fib and TTR-ol clearly induced a net increase in the baseline calcium signal, indicating a progressive accumulation of cytosolic calcium ([Fig. 6, C and G](#)).

Considering that the increase of cytosolic  $\text{Ca}^{2+}$  in oligomer- and fibril-exposed cells resulted from aggregate interaction with the cell membrane and, possibly, oligomer internalization, we hypothesized that in cells exposed to TTR-ol, the internalized species gained access to the  $\text{Ca}^{2+}$  stores in the SR, favoring  $\text{Ca}^{2+}$  exit to the cytosol, as was previously shown for the endoplasmic reticulum in a mouse neuronal cell line (16). Therefore, we studied whether the  $\text{Ca}^{2+}$  deposits in HL-1 were sensitive to cell exposure to TTR-ol, TTR-fib, and TTR-T4 by investigating the possible involvement of the Rya and IP<sub>3</sub> receptors, two well-known SR receptors that regulate  $\text{Ca}^{2+}$  handling in CMs. HL-1 cells were preincubated with Rya and 2-APB for 15 min to block the Rya and IP<sub>3</sub> receptors, respectively, before and during exposure to TTR-ol, TTR-fib, or TTR-T4. Under these conditions, the increase of intracellular  $\text{Ca}^{2+}$  was significantly reduced ([Fig. 5 B](#); [Table S1](#)), suggesting an involvement of the Rya and IP<sub>3</sub> receptors and hence of the SR  $\text{Ca}^{2+}$  stores. In automatic HL-1 cells, spontaneous calcium oscillations were eliminated by depletion of intracellular calcium stores with Rya and 2-APB ([Fig. 6, E–N](#)). Nonetheless, during Rya or 2-APB treatment, TTR-ol and

TTR-fib were still able to produce a modest yet visible increase of the baseline calcium signal ([Fig. 6, E and J](#)), in line with the effect observed in quiescent HL-1 cells ([Fig. 5 B](#)).

It is known that amyloid oligomers permeabilize the plasma membrane of exposed cells, favoring uncontrolled  $\text{Ca}^{2+}$  entry from the extracellular milieu either nonspecifically after disassembly of the membrane bilayer (46,47) and/or through the participation of specific  $\text{Ca}^{2+}$  channels (48,49). Therefore, we removed  $\text{Ca}^{2+}$  from the external solution to check whether and to what extent the CM plasma membrane, in addition to the SR one, was involved in the intracellular  $\text{Ca}^{2+}$  increase induced by TTR aggregates. Under these conditions, the increase of cytosolic  $\text{Ca}^{2+}$  in cells exposed to either TTR-ol or TTR-fib was significantly reduced ([Fig. 5 B](#) and [Table S1](#)). Spontaneous calcium oscillations were also eliminated in automatic HL-1 cells by removal of external  $\text{Ca}^{2+}$  ([Fig. 6, D–L](#)), in agreement with previous data (50). Similar to what was observed in the nonautomatic HL-1 cells ([Fig. 5 B](#)), exposure to either TTR-fib or TTR-ol enhanced the baseline calcium signal ([Fig. 6, D and H](#)). Thus,  $\text{Ca}^{2+}$  influx from the extracellular medium and release from the internal stores both contribute to the cytoplasmic  $\text{Ca}^{2+}$  increase induced by prefibrillar and fibrillar wtTTR.

### Effect of TTR aggregates on calcium cycling and the action potential profile of mouse ventricular myocytes

The enhanced intracellular  $\text{Ca}^{2+}$  levels in cells exposed to TTR-ol or TTR-fib led us to hypothesize that the presence of TTR aggregates could alter  $\text{Ca}^{2+}$  cycling and the membrane potential during myocyte contraction. To test this hypothesis, we measured  $\text{Ca}^{2+}$  transients in mouse ventricular CMs during contraction evoked by electrical stimulation.

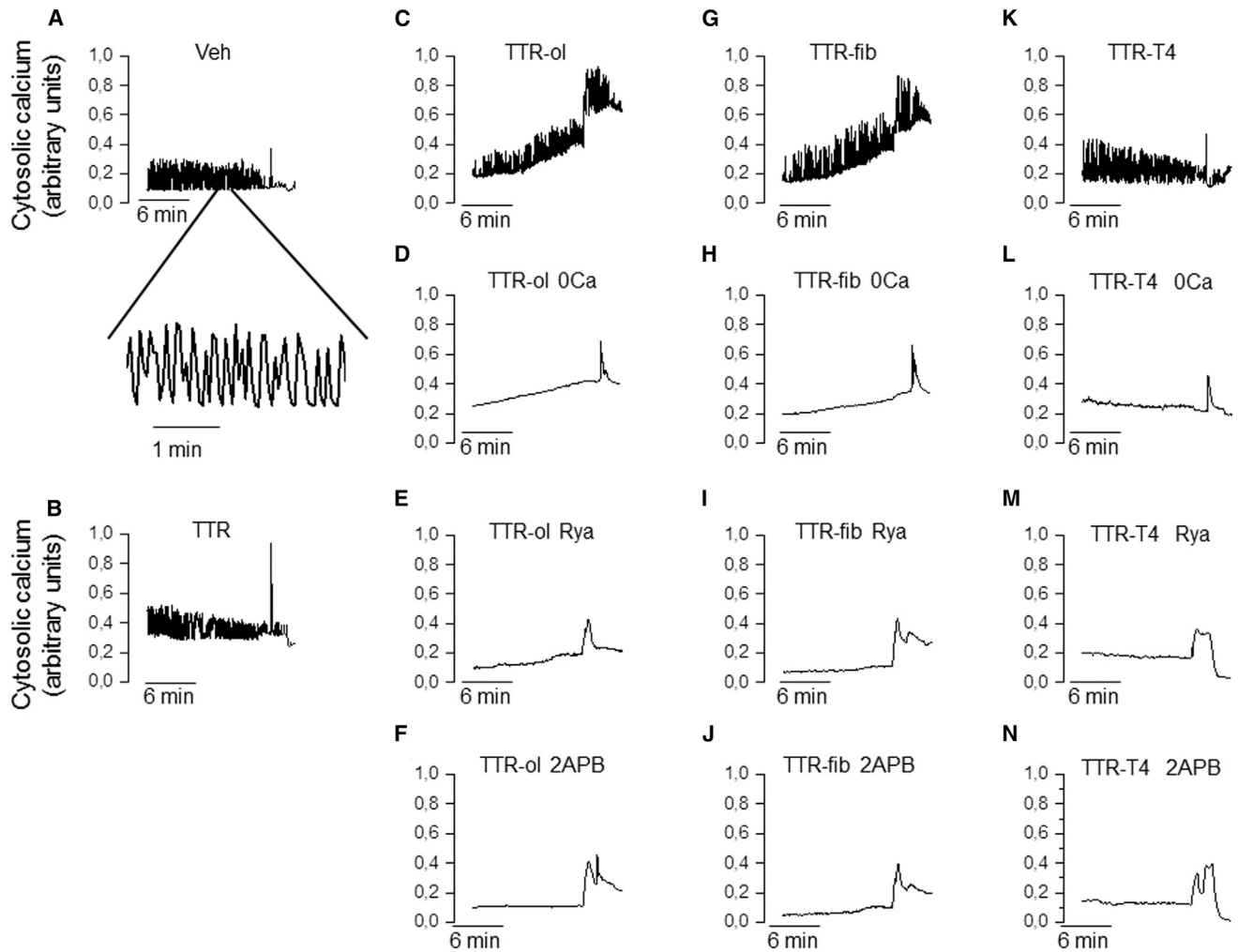
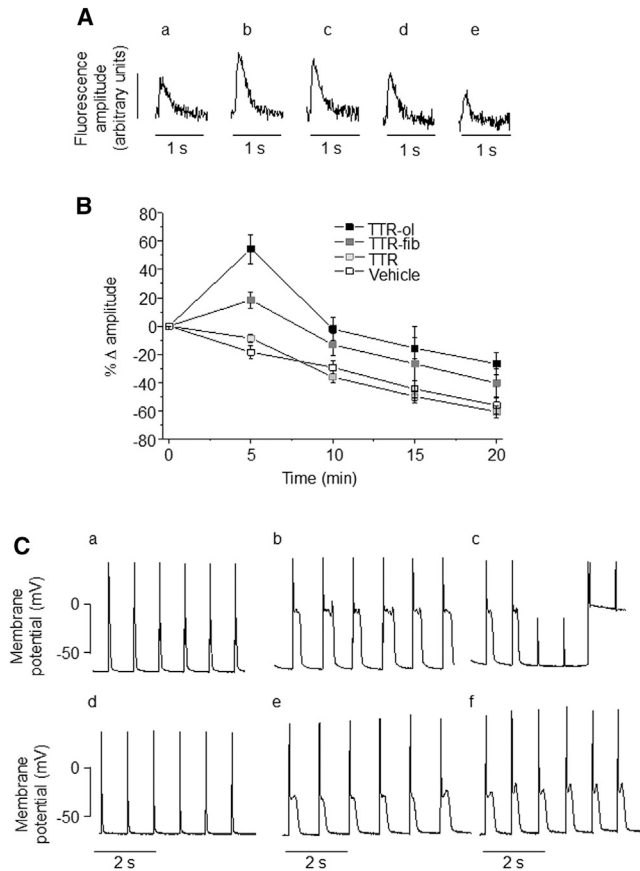


FIGURE 6 Effects of different TTR samples on cytoplasmic calcium levels in automatic HL-1 CMs. (A) Time course of cytosolic  $\text{Ca}^{2+}$  signals detected in automatic HL-1 CMs exposed to vehicle (A), 10  $\mu\text{M}$  TTR (B), TTR-ol (C), TTR-ol in  $\text{Ca}^{2+}$ -free medium (D), TTR-ol plus ryanodine (E), TTR-ol plus 2-APB (F), TTR-fib (G), TTR-fib in  $\text{Ca}^{2+}$ -free medium (H), TTR-fib plus ryanodine (I), TTR-fib plus 2-APB (J), TTR-T4 (K), TTR-T4 in  $\text{Ca}^{2+}$ -free medium (L), TTR-T4 plus ryanodine (M), or TTR-T4 plus 2-APB (N) for 20 min before SR depletion with 10 mM caffeine. Abbreviations: Veh, vehicle; TTR-ol, oligomeric transthyretin; TTR-fib, fibrillar transthyretin; TTR-T4, native TTR complex with thyroid hormone; TTR-ol 0 Ca, oligomeric TTR in  $\text{Ca}^{2+}$ -free medium; TTR-fib 0 Ca, fibrillar TTR in  $\text{Ca}^{2+}$ -free medium; TTR-T4 0 Ca, TTR-T4 in  $\text{Ca}^{2+}$ -free medium; TTR-ol Rya, oligomeric TTR plus ryanodine; TTR-ol 2-APB, oligomeric TTR plus 2-APB; TTR-fib Rya, fibrillar TTR plus ryanodine; TTR-fib 2-APB, fibrillar TTR plus 2-APB; TTR-T4 Rya, TTR-T4 plus ryanodine; TTR-T4 2-APB, TTR-T4 plus 2-APB.

As shown in Fig. 7 A, cell treatment with 10  $\mu\text{M}$  TTR-ol increased  $\text{Ca}^{2+}$  transient amplitudes after 5 min (b), 10 min (c), and 15 min (d) of exposure. At the same time, the mean fractional variations of the  $\text{Ca}^{2+}$  transient amplitude (Fig. 7 B) in cells exposed to TTR-ol were significantly different from those detected in cells exposed to TTR-T4 or to vehicle. We observed a similar effect in cells exposed to TTR-fib: the effect arose in the same time window, but its magnitude was significantly reduced as compared with that seen in cells exposed to TTR-ol (see Table S2 for statistical analysis). The reduced magnitude was consistent with the smaller cumulative calcium fractional variation induced by TTR-fib as compared with TTR-ol in HL-1 cells. This finding agrees with the  $\text{Ca}^{2+}$

release from the internal stores and the  $\text{Ca}^{2+}$  flux from the extracellular medium seen in HL-1 cells (see above). Other parameters of  $\text{Ca}^{2+}$  transient (baseline level, time to peak, and decay kinetics) were not modified (Tables S3–S5; Table 2).

Finally, to assess the consequences of the altered intracellular  $\text{Ca}^{2+}$  cycling on the membrane potential, we performed whole-cell recordings of the action potential on isolated mouse ventricular myocytes by adding TTR-ol or TTR-fib to the pipette solution. Under this condition, a clear prolongation of the action potential became evident 3 min after whole-cell access was gained. This persisted after 7 min and was characterized by a marked lengthening of the plateau phase (Fig. 7 C). The observed effect on the



**FIGURE 7** Effects of TTR variants on the calcium transient and action potential of mouse ventricular myocytes. (A) Representative fluorescence signals measured from ventricular CMs loaded with Fluo-4 and stimulated at a 1.0 Hz pacing frequency during exposure to oligomeric TTR for 0 (a), 5 (b), 10 (c), 15 (d), or 20 (e) min. (B) Time course of Ca<sup>2+</sup> transient amplitude variation, expressed as the mean fractional variation ( $\pm$  standard error of the mean) relative to the time zero amplitude in ventricular CMs exposed to vehicle ( $n = 18$ ), TTR-ol ( $n = 13$ ), TTR-fib ( $n = 19$ ), or wtTTR ( $n = 14$ ). The statistical analysis (ANOVA followed by Tukey's multiple-comparisons test) is reported in Table S2. (C) Representative action potential profiles measured from ventricular CMs recorded in whole-cell configuration (1.0 Hz pacing frequency) immediately after seal rupture (a and d) and after 3 or 7 min of exposure to a pipette solution containing 1.0  $\mu$ M TTR-ol (b and c) or TTR-fib (e and f).

membrane potential is in line with the increase of cytosolic Ca<sup>2+</sup> reported above and confirms the interference of oligomeric and fibrillar TTR with the electrophysiological properties of the investigated CMs.

## DISCUSSION

Cardiomyopathy is the most frequent and severe complication of TTR amyloidosis in both the familial (FAC) and senile (SSA) forms. The lack of effective pharmacological treatments for these conditions is due, at least in part, to the lack of information regarding the key factors underlying TTR misfolding and aggregation in tissue, as well as the molecular features of the biochemical, functional, and viability impairments of cardiac cells exposed to aggregated TTR. Presently, the cytotoxicity of amyloid aggregates, particularly those that arise early in the aggregation path, is considered to be one of the main factors responsible for cell functional and viability impairments (15,47), although cell sufferance can also result from the physical barrier to nutrient exchange posed by fibrillar deposits (51).

In this study, we investigated how different wtTTR forms, such as the nonamyloidogenic, stabilized T4-bound derivative and amyloidogenic TTR (including prefibrillar assemblies (TTR-ol) and mature fibrils (TTR-fib)) affect the viability and some biochemical parameters of exposed CMs. These data were added to those provided by electrophysiological experiments on the early functional alterations that occur in exposed cardiac cells in terms of Ca<sup>2+</sup> transients and membrane potential. In our experimental model, the TTR-fib sample contained a heterogeneous mixture of prefibrillar and fibrillar components as shown by dot immunostaining. This makes sense if one considers that cardiac cells are exposed to tissue deposits where TTR is aggregated in the fibrillar form, and that oligomeric and/or protofibrils entities can also be present either as intermediates in the aggregation path (12,13) and/or after leakage from the fibrillar deposits, as was previously reported for other aggregated proteins (17).

We initially characterized the aggregated forms used in this study by investigating in depth the path of TTR aggregation at pH 4.4 or 7.4, as well as aggregate morphology, by FT-IR, CR, DLS, and AFM. The aggregation of wtTTR, but not TTR-T4, at pH 4.4 displayed the well-known path, where early oligomers are progressively replaced by mature fibrils as long as aggregation proceeds. The protein did not aggregate at pH 7.4, even during long incubation times, as was previously reported (15). We then investigated whether, where, and how the different TTR aggregates were able to interact with the sarcolemma of the exposed cells. Prefibrillar TTR assemblies and TTR fibrils interacted with the

**TABLE 2** The 90% Decay Time Fractional Variation of Calcium Transient Relatives to Initial Values in Mice Ventricular Cardiomyocytes

Time (min)	Vehicle (mean $\pm$ SE) $n = 18$	TTR (mean $\pm$ SE) $n = 13$	TTR-ol (mean $\pm$ SE) $n = 14$	TTR-fib (mean $\pm$ SE) $n = 19$
0	$1.1 \times 10^{-6} \pm 9.1 \times 10^{-7}$	$2.0 \times 10^{-7} \pm 3.1 \times 10^{-7}$	$8.3 \times 10^{-7} \pm 1.0 \times 10^{-6}$	$4.4 \times 10^{-8} \pm 1.9 \times 10^{-7}$
5	$15.7 \pm 12.3$	$-7.5 \pm 8.7$	$14.0 \pm 12.6$	$10.4 \pm 3.9$
10	$13.9 \pm 12.0$	$1.3 \pm 10.3$	$17.0 \pm 15.3$	$13.2 \pm 5.1$
15	$30.1 \pm 18.0$	$16.2 \pm 10.3$	$40.2 \pm 23.3$	$25.4 \pm 10.9$
20	$122.4 \pm 31.4$	$115.7 \pm 25.8$	$202.8 \pm 81.4$	$122.3 \pm 25.1$

plasma membrane of CMs, and such interactions required the negatively charged sialic acid moiety of the ganglioside GM1, a key lipid raft component, although we cannot exclude some contribution coming from the sialic acid residues bound to membrane glycoproteins. In this regard, there are some clear qualitative commonalities with data obtained in other cell types (namely, neurons) and with aggregates grown from different peptides/proteins: amyloid aggregation and aggregate recruitment are favored by GM1-rich sites of the cell membrane (48,52,53) and, more generally, by negatively charged surfaces (54–58). This observation also leads us to speculate that an increase in GM1 content in aged CMs could favor TTR aggregation in SSA, as was previously shown in amyloid-positive synaptosomes from brains with Alzheimer's disease (54). However, as far as we know, no data regarding the GM1 content in aged CMs are available. Under our experimental conditions, the colocalization analysis showed that the fibrillar component promoted a higher GM1 recruitment than the prefibrillar component, suggesting a higher activity of the fibrils upon cell membrane uptake by raft components and subsequent membrane damage. Accordingly, a recent study (30) suggested that amyloid toxicity is mediated by cellular factors that interact with protofibrils and fibrils, inducing further protein fibrillization on the cell surface that in turn triggers a cascade of intracellular events downstream that compromise cell survival. The importance of lipid rafts in TTR recruitment by the plasma membrane of exposed cells is indirectly confirmed by a recent study in which Manral and Reixach (31) reported that a reduction of membrane cholesterol, a key component of lipid rafts, significantly impaired the interaction and subsequent internalization of two TTR variants (I122V and T119M) with the plasma membrane of exposed CMs (the AC16 line). Although the authors exposed cells to soluble, nonaggregated proteins, they were aware of the difficulty of assessing precisely which TTR species are involved in cell damage. They speculated about the possibility that the samples of their soluble amyloidogenic V121I TTR contained tiny amounts of oligomer populations that would interact preferentially with the exposed cells. If so, their conditions would resemble those used in our well-controlled approach.

TTR-ol and TTR-fib displayed significant cytotoxicity, but they did not result in cell death under our conditions, in accordance with their abilities to interact with the plasma membrane, to be internalized (in the case of TTR-ol), to induce intracellular ROS production, and to alter intracellular  $\text{Ca}^{2+}$  homeostasis and the mitochondrial membrane potential. The latter effects were, at least in part, the consequence of membrane permeabilization to calcium; in fact, increase in intracellular  $\text{Ca}^{2+}$  concentration and mitochondrial membrane potential perturbation were not seen in cells cultured in  $\text{Ca}^{2+}$ -free medium or exposed to the stabilized TTR-T4, which was unable to bind to the plasma membrane. The hampered  $\text{Ca}^{2+}$  increase in cells treated with in-

hibitors of the Rya and IP3 receptors before exposure to aggregated TTR suggests that such an increase depends, at least in part, on the release from SR stores through either receptor. Similar observations were previously made in mouse neuronal cells exposed to TTR oligomers (16), suggesting the existence of shared basic alterations induced by TTR aggregates in different cell types and a possible pathophysiological basis for multiorgan failure in TTR amyloidosis. In our model, it is possible that the increased  $\text{Ca}^{2+}$  initially came from the extracellular medium and only subsequently from the intracellular stores by  $\text{Ca}^{2+}$ -induced calcium release, an important mechanism of  $\text{Ca}^{2+}$  handling in cardiac cells (59). We cannot exclude the possibility that the effects observed at the mitochondrial and SR membranes result, at least in part, from the interaction with the internalized oligomers; however, the same effects were also found in cells exposed to TTR-fib, where intracellular oligomers were absent. More likely, the mitochondrial membrane depolarization resulted from the increased levels of free intracellular  $\text{Ca}^{2+}$ , as reported in other cases (60). In the case of TTR-fib, which does not penetrate inside the cells, a different mechanism, either alternative or additive, can be hypothesized. This could involve fibril interaction with death receptors or  $\text{Ca}^{2+}$  channels, as was previously shown for amyloid fibrils grown from Sup35NM (27) or ataxin-3 (48). This scenario supports the idea that in TTR amyloidosis, same disturbance of cell/tissue function by the deposits of fibrillar material results not only from a mechanical alteration of proper oxygen and nutrient exchange, but also from more subtle biochemical and physiological modifications resulting from the interaction of deposited fibrils and/or leaked oligomers with surrounding cells. Several lines of evidence implicate amyloid oligomers as the main cytotoxic species, even though not all oligomers are cytotoxic (61,62). However, the cytotoxicity of amyloid fibrils is not surprising since it has been reported repeatedly (19–23). In addition, given the high complexity of the fibrillation process, and considering the overall dynamics of the assembly and disassembly of toxic amyloid species, the possibility that toxicity is displayed by different conformers should not be disregarded. Moreover, it has also been suggested that the ongoing aggregation process, rather than a clearly defined aggregate, is responsible for amyloid toxicity (30,63).

Our findings regarding  $\text{Ca}^{2+}$  dyshomeostasis in exposed CMs reveal the occurrence of early effects, which likely precede or parallel those that affect cell viability and mitochondrial physiology. In cell cultures, all of these effects developed within minutes from cell exposure to the aggregates, as shown by the temporal dynamics of the  $\text{Ca}^{2+}$  levels and action potential recordings. A similar time course of cytoplasmic  $\text{Ca}^{2+}$  increase was previously observed in peripheral sensory neurons exposed to TTR aggregates, where the effects were mediated by a gain of function of different ion channels, namely, voltage-gated calcium and sodium channels and transient receptor potential M8 channels

(14). The question of whether in our setting the enhanced intracellular  $\text{Ca}^{2+}$  resulted from similar modifications deserves further investigation. In line with this observation, our findings regarding the perturbation of intracellular  $\text{Ca}^{2+}$  homeostasis do not exclude (or may also concur with) the possibility of multiple modifications of different ion channels and/or pumps, which altogether contribute to define the functional profile of CMs. However, a comprehensive exploration of each specific ionic modification potentially induced by TTR variants would require dedicated investigations beyond the scope of this study. Interestingly, in sensory neurons, one of the mechanisms that have been proposed to explain the  $\text{Ca}^{2+}$  increase is a TTR interaction with cholesterol-rich regions of membranes that are able to promote ion channel opening. This hypothesis is in line with previous findings (31,55,64) and with the data presented here, which show a preferential interaction of TTR aggregates with GM1-rich sites, presumably in lipid rafts. Of note, GM1-rich sites have been shown to colocalize with and modulate ion channel function in the plasma membrane of different cell types (65–70), and with the sodium calcium exchanger in the nuclear envelope of CMs (71).

Besides cell viability and mitochondrial efficiency, the increase in  $\text{Ca}^{2+}$  transient amplitude observed in electrically stimulated ventricular CMs exposed to TTR aggregates is in agreement with their ability to mobilize cytosolic  $\text{Ca}^{2+}$ . Indeed, in CMs, a complex network involving plasmalemma, SR receptors (namely, Rya, but also IP3 receptors), and mitochondria is responsible for fine-tuning cytosolic  $\text{Ca}^{2+}$  (72–74). In this interplay, the mitochondria serve as an efficient dynamic buffer of the  $\text{Ca}^{2+}$  released during contraction. The interplay that occurs inside cells among oxidative metabolism, calcium levels, ATP and ROS production, and protein aggregation was previously outlined (74). It is possible that ionic mechanisms that serve this function at the mitochondrial membrane are impaired by TTR aggregate-induced membrane depolarization, thus contributing to the cytoplasmic  $\text{Ca}^{2+}$  increase. Regardless of the source of  $\text{Ca}^{2+}$  accumulation inside the CMs, this effect is expected invariably to have relevant consequences in terms of the generation and propagation of electrical impulses. Indeed, an increase in intracellular calcium concentration is a common feature of several acquired or congenital cardiomyopathies: for the sake of comparison, a 40% increase in diastolic  $\text{Ca}^{2+}$  levels was measured in CMs from patients with hypertrophic cardiomyopathy as compared with control cells (75). Such an increase is sufficient to predispose CMs to contractile dysfunction and the occurrence of arrhythmogenic mechanisms (74). Accordingly, action potential recordings in mouse ventricular myocytes exposed to TTR aggregates showed a remarkable prolongation of repolarization with a pronounced increase of the plateau level. Both events are suggestive of increased cytosolic  $\text{Ca}^{2+}$  levels, in agreement with our findings regarding TTR aggregate-induced

$\text{Ca}^{2+}$  accumulation and with previous studies in isolated CMs (76).

## CONCLUSION

Taken together, our results indicate that alterations of the mechanisms that control intracellular  $\text{Ca}^{2+}$  homeostasis and prolong the duration of the action potential may alter the functional properties of CMs, favoring the development of cellular arrhythmias. In addition to further supporting the idea that specific cellular abnormalities are induced by TTR aggregates in the heart parenchyma, these effects may also represent a basis for the occurrence of rhythm disturbances and conduction alterations often seen in patients with TTR amyloidosis.

## SUPPORTING MATERIAL

One figure and five tables are available at [http://www.biophysj.org/biophysj/supplemental/S0006-3495\(16\)30803-7](http://www.biophysj.org/biophysj/supplemental/S0006-3495(16)30803-7).

## AUTHOR CONTRIBUTIONS

L.S.: conception and design, collection and/or assembly of data, data analysis and interpretation, manuscript writing. M.B.: conception and design, collection and/or assembly of data, data analysis and interpretation, manuscript writing, financial support. V.S.: collection and assembly of data, calcium transient. M.L.: collection and assembly of data, biochemical and biophysical analysis. A.N.: collection and assembly of data, FTIR analysis. D.N.: collection and assembly of data, confocal imaging. S.M.D.: collection and assembly of data, FTIR analysis. A.R.: collection and assembly of data, AFM analysis. A.P.: collection and assembly of data, AFM analysis. S.G.: collection and assembly of data. E.G.: collection and assembly of data, calcium transient. G.M.: data analysis and interpretation, calcium transient. V.B.: data analysis and interpretation. S.R.: collection and assembly of data. E.C.: conception and design, data analysis and interpretation, manuscript writing, financial support. M.S.: conception and design, data analysis and interpretation, manuscript writing, financial support.

## ACKNOWLEDGMENTS

This work was supported by grants from the Ente Cassa di Risparmio di Firenze, Project Lipid Rafts, and from the Italian MIUR, PRIN 2009 (2009KN2FBM\_002).

## REFERENCES

- Sanbe, A., H. Osinska, ..., J. Robbins. 2004. Desmin-related cardiomyopathy in transgenic mice: a cardiac amyloidosis. *Proc. Natl. Acad. Sci. USA.* 101:10132–10136.
- Willis, M. S., and C. Patterson. 2013. Proteotoxicity and cardiac dysfunction—Alzheimer's disease of the heart? *N. Engl. J. Med.* 368:455–464.
- Rapezzi, C., G. Merlini, ..., S. Perlini. 2009. Systemic cardiac amyloidoses: disease profiles and clinical courses of the 3 main types. *Circulation.* 120:1203–1212.
- Snyder, E. L., W. C. Nichols, ..., M. D. Benson. 1989. Direct evidence for the hereditary nature of senile cardiac (systemic) amyloidosis. *Am. J. Hum. Genet.* 45 (suppl.):A220.

5. White, J. T., and J. W. Kelly. 2001. Support for the multigenic hypothesis of amyloidosis: the binding stoichiometry of retinol-binding protein, vitamin A, and thyroid hormone influences transthyretin amyloidogenicity in vitro. *Proc. Natl. Acad. Sci. USA.* 98:13019–13024.
6. Ando, Y., M. Nakamura, and S. Araki. 2005. Transthyretin-related familial amyloidotic polyneuropathy. *Arch. Neurol.* 62:1057–1062.
7. Rapezzi, C., C. C. Quarta, ..., A. Branzi. 2010. Transthyretin-related amyloidoses and the heart: a clinical overview. *Nat. Rev. Cardiol.* 7:398–408.
8. Quintas, A., M. J. Saraiva, and R. M. Brito. 1997. The amyloidogenic potential of transthyretin variants correlates with their tendency to aggregate in solution. *FEBS Lett.* 418:297–300.
9. Johnson, S. M., R. L. Wiseman, ..., J. W. Kelly. 2005. Native state kinetic stabilization as a strategy to ameliorate protein misfolding diseases: a focus on the transthyretin amyloidoses. *Acc. Chem. Res.* 38:911–921.
10. Hou, X., M.-I. Aguilar, and D. H. Small. 2007. Transthyretin and familial amyloidotic polyneuropathy. Recent progress in understanding the molecular mechanism of neurodegeneration. *FEBS J.* 274:1637–1650.
11. Miroy, G. J., Z. Lai, ..., J. W. Kelly. 1996. Inhibiting transthyretin amyloid fibril formation via protein stabilization. *Proc. Natl. Acad. Sci. USA.* 93:15051–15056.
12. Reixach, N., S. Deechongkit, ..., J. N. Buxbaum. 2004. Tissue damage in the amyloidoses: Transthyretin monomers and nonnative oligomers are the major cytotoxic species in tissue culture. *Proc. Natl. Acad. Sci. USA.* 101:2817–2822.
13. Sousa, M. M., I. Cardoso, ..., M. J. Saraiva. 2001. Deposition of transthyretin in early stages of familial amyloidotic polyneuropathy: evidence for toxicity of nonfibrillar aggregates. *Am. J. Pathol.* 159:1993–2000.
14. Gasperini, R. J., X. Hou, ..., D. H. Small. 2011. TRPM8 and Na<sub>v</sub>1.8 sodium channels are required for transthyretin-induced calcium influx in growth cones of small-diameter TrkA-positive sensory neurons. *Mol. Neurodegener.* 6:19–30.
15. Hou, X., H. C. Parkington, ..., D. H. Small. 2007. Transthyretin oligomers induce calcium influx via voltage-gated calcium channels. *J. Neurochem.* 100:446–457.
16. Teixeira, P. F., F. Cerca, ..., M. J. Saraiva. 2006. Endoplasmic reticulum stress associated with extracellular aggregates. Evidence from transthyretin deposition in familial amyloid polyneuropathy. *J. Biol. Chem.* 281:21998–22003.
17. Misumi, Y., M. Ueda, ..., M. Uchino. 2012. Relationship between amyloid deposition and intracellular structural changes in familial amyloidotic polyneuropathy. *Hum. Pathol.* 43:96–104.
18. Sousa, M. M., R. Fernandes, ..., M. J. Saraiva. 2002. Evidence for early cytotoxic aggregates in transgenic mice for human transthyretin Leu55Pro. *Am. J. Pathol.* 161:1935–1948.
19. Gharibyan, A. L., V. Zamotin, ..., L. A. Morozova-Roche. 2007. Lysozyme amyloid oligomers and fibrils induce cellular death via different apoptotic/necrotic pathways. *J. Mol. Biol.* 365:1337–1349.
20. Mossuto, M. F., A. Dhulesia, ..., X. Salvatella. 2010. The non-core regions of human lysozyme amyloid fibrils influence cytotoxicity. *J. Mol. Biol.* 402:783–796.
21. Pieri, L., K. Madiona, ..., R. Melki. 2012. Fibrillar  $\alpha$ -synuclein and huntingtin exon 1 assemblies are toxic to the cells. *Biophys. J.* 102:2894–2905.
22. Mocanu, M. M., C. Ganea, ..., Z. Gazova. 2014. Polymorphism of hen egg white lysozyme amyloid fibrils influences the cytotoxicity in LLC-PK1 epithelial kidney cells. *Int. J. Biol. Macromol.* 65:176–187.
23. Harte, N. P., I. Klyubin, ..., K. H. Mok. 2015. Amyloid oligomers and mature fibrils prepared from an innocuous protein cause diverging cellular death mechanisms. *J. Biol. Chem.* 290:28343–28352.
24. Fukunaga, S., H. Ueno, ..., K. Matsuzaki. 2012. GMI cluster mediates formation of toxic A $\beta$  fibrils by providing hydrophobic environments. *Biochemistry.* 51:8125–8131.
25. Lee, Y. J., R. Savtchenko, ..., I. V. Baskakov. 2011. Molecular structure of amyloid fibrils controls the relationship between fibrillar size and toxicity. *PLoS One.* 6:e20244.
26. Pieri, L., M. Bucciantini, ..., M. Stefani. 2006. The yeast prion Ure2p native-like assemblies are toxic to mammalian cells regardless of their aggregation state. *J. Biol. Chem.* 281:15337–15344.
27. Bucciantini, M., D. Nosi, ..., M. Stefani. 2012. Toxic effects of amyloid fibrils on cell membranes: the importance of ganglioside GMI. *FASEB J.* 26:818–831.
28. Leri, M., D. Nosi, ..., M. Bucciantini. 2016. The polyphenol Oleuropein aglycone hinders the growth of toxic transthyretin amyloid assemblies. *J. Nutr. Biochem.* 30:153–166.
29. Leri, M., F. Bemporad, ..., M. Bucciantini. 2016. Molecular insights into cell toxicity of a novel familial amyloidogenic variant of  $\beta$ 2-microglobulin. *J. Cell. Mol. Med.* 20:1443–1456.
30. Jan, A., O. Adolfsson, ..., H. A. Lashuel. 2011. Abeta42 neurotoxicity is mediated by ongoing nucleated polymerization process rather than by discrete Abeta42 species. *J. Biol. Chem.* 286:8585–8596.
31. Manral, P., and N. Reixach. 2015. Amyloidogenic and non-amyloidogenic transthyretin variants interact differently with human cardiomyocytes: insights into early events of non-fibrillar tissue damage. *Biosci. Rep.* 35:e00172.
32. Natalello, A., R. U. Mattoo, ..., S. M. Doglia. 2013. Biophysical characterization of two different stable misfolded monomeric polypeptides that are chaperone-amenable substrates. *J. Mol. Biol.* 425:1158–1171.
33. Natalello, A., D. Ami, ..., S. M. Doglia. 2012. Biophysical characterization of Met-G-CSF: effects of different site-specific pegylations on protein stability and aggregation. *PLoS One.* 7:e42511.
34. Claycomb, W. C., N. A. Lanson, Jr., ..., N. J. Izzo, Jr. 1998. HL-1 cells: a cardiac muscle cell line that contracts and retains phenotypic characteristics of the adult cardiomyocyte. *Proc. Natl. Acad. Sci. USA.* 95:2979–2984.
35. Berlinguer-Palmini, R., R. Narducci, ..., G. Mannaioni. 2014. Arrays of microLEDs and astrocytes: biological amplifiers to optogenetically modulate neuronal networks reducing light requirement. *PLoS One.* 9:e108689. <http://dx.doi.org/10.1371/journal.pone.0108689>.
36. Sartiani, L., E. Cerbai, ..., A. Mugelli. 2004. Prenatal exposure to carbon monoxide affects postnatal cellular electrophysiological maturation of the rat heart: a potential substrate for arrhythmogenesis in infancy. *Circulation.* 109:419–423.
37. Wang, S. S., D. L. Rymer, and T. A. Good. 2001. Reduction in cholesterol and sialic acid content protects cells from the toxic effects of beta-amyloid peptides. *J. Biol. Chem.* 276:42027–42034.
38. Zinchuk, O., and V. Zinchuk. 2006. Dynamics of cellular responses studied by quantitative colocalization analysis. *Microsc. Anal. (Am.).* 20:S13–S15.
39. Ami, D., S. Ricagno, ..., A. Natalello. 2012. Structure, stability, and aggregation of  $\beta$ -2 microglobulin mutants: insights from a Fourier transform infrared study in solution and in the crystalline state. *Biophys. J.* 102:1676–1684.
40. Cordeiro, Y., J. Kraineva, ..., D. Foguel. 2006. Fourier transform infrared spectroscopy provides a fingerprint for the tetramer and for the aggregates of transthyretin. *Biophys. J.* 91:957–967.
41. Zandomenighi, G., M. R. H. Krebs, ..., M. Fändrich. 2004. FTIR reveals structural differences between native beta-sheet proteins and amyloid fibrils. *Protein Sci.* 13:3314–3321.
42. Pires, R. H., Á. Karsai, ..., M. S. Kellermayer. 2012. Distinct annular oligomers captured along the assembly and disassembly pathways of transthyretin amyloid protofibrils. *PLoS One.* 7:e44992. <http://dx.doi.org/10.1371/journal.pone.0044992>.
43. Hou, X., A. Mechler, ..., D. H. Small. 2008. Cholesterol and anionic phospholipids increase the binding of amyloidogenic transthyretin to lipid membranes. *Biochim. Biophys. Acta.* 1778:198–205.
44. Wang, X., W. Wang, ..., X. Zhu. 2014. Oxidative stress and mitochondrial dysfunction in Alzheimer's disease. *Biochim. Biophys. Acta.* 1842:1240–1247.

45. Sartiani, L., P. Bochet, ..., R. Fischmeister. 2002. Functional expression of the hyperpolarization-activated, non-selective cation current I(f) in immortalized HL-1 cardiomyocytes. *J. Physiol.* 545:81–92.
46. Glabe, C. G., and R. Kaye. 2006. Common structure and toxic function of amyloid oligomers implies a common mechanism of pathogenesis. *Neurology*. 66 (2, Suppl 1):S74–S78.
47. Pellistri, F., M. Bucciantini, ..., M. Stefani. 2013. Different ataxin-3 amyloid aggregates induce intracellular Ca<sup>2+</sup> deregulation by different mechanisms in cerebellar granule cells. *Biochim. Biophys. Acta.* 1833:3155–65.
48. Um, J. W., A. C. Kaufman, ..., S. M. Strittmatter. 2013. Metabotropic glutamate receptor 5 is a coreceptor for Alzheimer A $\beta$  oligomer bound to cellular prion protein. *Neuron*. 79:887–902.
49. Campioni, S., B. Mannini, ..., F. Chiti. 2010. A causative link between the structure of aberrant protein oligomers and their toxicity. *Nat. Chem. Biol.* 6:140–147.
50. Sokolov, Y., J. A. Kozak, ..., J. E. Hall. 2006. Soluble amyloid oligomers increase bilayer conductance by altering dielectric structure. *J. Gen. Physiol.* 128:637–647.
51. Ladiwala, A. R., J. Litt, ..., P. M. Tessier. 2012. Conformational differences between two amyloid  $\beta$  oligomers of similar size and dissimilar toxicity. *J. Biol. Chem.* 287:24765–24773.
52. Stefani, M. 2012. Structural features and cytotoxicity of amyloid oligomers: implications in Alzheimer's disease and other diseases with amyloid deposits. *Prog. Neurobiol.* 99:226–245.
53. Xue, W. F., A. L. Hellewell, ..., S. E. Radford. 2009. Fibril fragmentation enhances amyloid cytotoxicity. *J. Biol. Chem.* 284:34272–34282.
54. Wakabayashi, M., and K. Matsuzaki. 2009. Ganglioside-induced amyloid formation by human islet amyloid polypeptide in lipid rafts. *FEBS Lett.* 583:2854–2858.
55. Yamamoto, N., T. Matsubara, T. Sato, and K. Yanagisawa. 2008. Age-dependent high-density clustering of GM1 ganglioside at presynaptic neuritic terminals promotes amyloid  $\beta$ -protein fibrillogenesis. *Biochim. Biophys. Acta.* 1778:2717–2726.
56. Hou, X., A. Mechler, ..., D. H. Small. 2008. Cholesterol and anionic phospholipids increase the binding of amyloidogenic transthyretin to lipid membranes. *Biochim. Biophys. Acta.* 1778:198–205.
57. Noborn, F., P. O'Callaghan, ..., J. P. Li. 2011. Heparan sulfate/heparin promotes transthyretin fibrillization through selective binding to a basic motif in the protein. *Proc. Natl. Acad. Sci. USA.* 108:5584–5589.
58. Bourgault, S., J. P. Solomon, ..., J. W. Kelly. 2011. Sulfated glycosaminoglycans accelerate transthyretin amyloidogenesis by quaternary structural conversion. *Biochemistry*. 50:1001–1015.
59. Calamai, M., and F. S. Pavone. 2013. Partitioning and confinement of GM1 ganglioside induced by amyloid aggregates. *FEBS Lett.* 587:1385–1391.
60. Fabiato, A. 1983. Calcium-induced release of calcium from the cardiac sarcoplasmic reticulum. *Am. J. Physiol.* 245:C1–C14.
61. Ferreira, E., C. R. Oliveira, and C. M. Pereira. 2008. The release of calcium from the endoplasmic reticulum induced by amyloid-beta and prion peptides activates the mitochondrial apoptotic pathway. *Neurobiol. Dis.* 30:331–342.
62. Evangelisti, E., C. Cecchi, ..., M. Stefani. 2012. Membrane lipid composition and its physicochemical properties define cell vulnerability to aberrant protein oligomers. *J. Cell Sci.* 125:2416–2427.
63. Hubin, E., N. A. van Nuland, ..., K. Pauwels. 2014. Transient dynamics of A $\beta$  contribute to toxicity in Alzheimer's disease. *Cell. Mol. Life Sci.* 71:3507–3521.
64. Furian, A. F., Y. D. Rattmann, ..., C. F. Mello. 2009. Nitric oxide and potassium channels mediate GM1 ganglioside-induced vasorelaxation. *Naunyn Schmiedebergs Arch. Pharmacol.* 380:487–495.
65. Wang, J., Z. H. Lu, ..., G. Wu. 2009. Cross-linking of GM1 ganglioside by galectin-1 mediates regulatory T cell activity involving TRPC5 channel activation: possible role in suppressing experimental autoimmune encephalomyelitis. *J. Immunol.* 182:4036–4045.
66. Wu, G., Z. H. Lu, ..., D. Bleich. 2011. Ganglioside GM1 deficiency in effector T cells from NOD mice induces resistance to regulatory T-cell suppression. *Diabetes*. 60:2341–2349.
67. Qiao, G. F., Z. F. Cheng, ..., B. Y. Li. 2008. GM1 ganglioside contributes to retain the neuronal conduction and neuronal excitability in visceral and baroreceptor afferents. *J. Neurochem.* 106:1637–1645.
68. Wu, G., Z. H. Lu, ..., R. W. Ledeen. 2007. Induction of calcium influx through TRPC5 channels by cross-linking of GM1 ganglioside associated with alpha5beta1 integrin initiates neurite outgrowth. *J. Neurosci.* 27:7447–7458.
69. Susuki, K., H. Baba, ..., N. Yuki. 2007. Gangliosides contribute to stability of paranodal junctions and ion channel clusters in myelinated nerve fibers. *Glia*. 55:746–757.
70. Hohendanner, F., A. D. McCulloch, ..., A. P. Michailova. 2014. Calcium and IP3 dynamics in cardiac myocytes: experimental and computational perspectives and approaches. *Front. Pharmacol.* 5:35.
71. Endo, M. 2006. Calcium ion as a second messenger with special reference to excitation-contraction coupling. *J. Pharmacol. Sci.* 100:519–524.
72. Signore, S., A. Sorrentino, ..., M. Rota. 2013. Inositol 1, 4, 5-trisphosphate receptors and human left ventricular myocytes. *Circulation*. 128:1286–1297.
73. Yang, K. C., M. G. Bonini, and S. C. Dudley, Jr. 2014. Mitochondria and arrhythmias. *Free Radic. Biol. Med.* 71:351–361.
74. Squier, T. C. 2001. Oxidative stress and protein aggregation during biological aging. *Exp. Gerontol.* 36:1539–1550.
75. Coppini, R., C. Ferrantini, ..., A. Mugelli. 2013. Late sodium current inhibition reverses electromechanical dysfunction in human hypertrophic cardiomyopathy. *Circulation*. 127:575–584.
76. Carmeliet, E. 2004. Intracellular Ca(2+) concentration and rate adaptation of the cardiac action potential. *Cell Calcium*. 35:557–573.